Journal of Power Sources 273 (2015) 404–412

Contents lists available at ScienceDirect

Journal of Power Sources

journal homepage: www.elsevier.com/locate/jpowsour

Improving the microstructure and electrochemical performance of carbon nanofibers containing graphene-wrapped silicon nanoparticles as a Li-ion battery anode

So Yeun Kim [a], Kap Seung Yang [b, *], Bo-Hye Kim [c, **]

[a] Department of Advanced Chemicals & Engineering, Chonnam National University, 300 Yongbong-dong, Gwangju, Republic of Korea
[b] Department of Polymer Engineering, Graduate School, Alan G. MacDiarmid Energy Research Institute, Chonnam National University, 300 Yongbong-dong, Gwangju, Republic of Korea
[c] Division of Science Education, Daegu University, 201 Daegudae-ro, Gyeongsan-si, Gyeongsangbuk-do, Republic of Korea

HIGHLIGHTS

- Preparation of graphene-wrapped Si nanoparticles embedded in carbon composite nanofibers.
- Investigation of the morphological characteristics, textual structure, and electrochemical performance of the CCNFs with G/Si.
- Development of CCNFs with G/Si as a promising anode material with a high specific capacity and good cycle performance.

ARTICLE INFO

Article history:
Received 10 July 2014
Received in revised form
5 September 2014
Accepted 16 September 2014
Available online 28 September 2014

Keywords:
Graphene-wrapped Si nanoparticle
Carbon nanofiber
Electrospinning
Lithium ion battery

ABSTRACT

A novel anode material for lithium-ion batteries, graphene-wrapped Si nanoparticles (NPs) embedded in carbon composite nanofibers (CCNFs) with G/Si, is fabricated by electrospinning and subsequent thermal treatment. In CCNFs with G/Si, Si NPs are distributed and preserved inside the CNF surface because the graphene wrapping the Si NPs help prevent agglomeration and ensure a good dispersion of Si NPs inside the CNF matrix. 20-GSP prepared from a weight ratio of 20 wt% of G/Si to polyacrylonitrile exhibits stable capacity retention and a reversible capacity of above 600 mAh g^{-1} up to 100 cycles. The high cycling performance and superior reversible capacity of the 20-GSP anode can be attributed to the one-dimensional nanofibrous structure with non-agglomerated Si NPs in the CNF matrix, which promotes charge transfer, maintains a stable electrical contact, and buffers the Si volume expansion.

1. Introduction

Recently, Si [1–4], Sn [5–8], and transition metal oxides [9–19] with superior capacity have been investigated as active anodes of lithium-ion batteries (LIBs) to meet the increasing demands in portable devices and electric vehicles for high energy density and long-term cycle performance. Of them, Si has attracted research attention as a valuable material of Si–Li alloy anode materials because of its highest known capacity (4200 mAh g^{-1}), acceptable cost, and low alloy potential [19]. However, Si anodes show large volume changes and agglomeration of Si particles during the insertion and de-insertion processes with lithium, leading to pulverization of the anode and electrical detachment of active materials, and thus a rapid capacity fade and a short cycle life [20,21]. To overcome this problem, many studies have been proposed to accommodate the large volume change of Si for an excellent anode material with long cycle life. One of the many efforts to mitigate the pulverization and enhance the structural stability is to prepare various Si/carbon composite anodes, which can combine the advantageous properties of carbon's long cycle life and silicon's high Li storage capacity for high electrochemical performance of LIBs. The carbon materials can buffer the crystallographic volume changes of the Si particles and provide good electrical contact during charging/discharging, thereby preventing the deterioration of the Si material and the disintegration of the electrode [22–27].

Recent studies suggest that electrospun carbon nanofibers (CNFs) containing Si nanoparticles (NPs) could be a promising anode candidate material in which the carbon layer on the Si NPs

* Corresponding author. Tel.: +82 62 530 0774; fax: +82 62 530 1779.
** Corresponding author. Tel.: +82 53 850 6982; fax: +82 53 850 6989.
E-mail addresses: ksyang@chonnam.ac.kr (K.S. Yang), bohye@daegu.ac.kr (B.-H. Kim).

http://dx.doi.org/10.1016/j.jpowsour.2014.09.109
0378-7753/

can not only buffer the volume change because of the amorphous structure of the hard carbon, but also enhance the conductivity as an electrochemically active material [28–33]. Furthermore, large surface areas with shallow pores in the CNFs increase the contact area between the electrolyte and electrode, the rate of lithium insertion/extraction, and the diffusion kinetics of the lithium ions [23,31,32]. However, Si NPs have shown difficulties in homogeneous dispersion because of the agglomeration to form clusters on the fiber surface of the Si/CNF composites. The Si clusters exposed on the surface lead to Si pulverization and capacity fading during the continuous lithium charge/discharge. Consequently, a new method is required to prepare well-dispersed and embedded Si NPs in a CNF matrix in order to improve the overall electrochemical performance of LIBs with larger capacity, higher efficient, longer cycle life, and better safety.

The purpose of this study is to develop electrospun carbon composite nanofibers (CCNFs) with well-dispersed, graphene-wrapped Si NPs (G/Si) as alternative anode material with a high specific capacity, good reversibility, and excellent cycle retention. We prepare G/Si composites by wrapping Si NPs with graphene oxide (GO), followed by a hybrid assembly and GO reduction. Specifically, the electrostatic interactions and chemical functionalization of GO and modified Si NPs help to prevent aggregation of Si NPs and facilitate the good dispersion of Si NPs on GO sheets. The CCNFs with G/Si are produced by incorporating G/Si composites into PAN through one-step electrospinning and subsequent thermal treatment, and their electrochemical properties as an LIB anode are investigated. As a result, CCNFs with G/Si-based anodes exhibit good rate performance and a reversible capacity of above 600 mAh g^{-1} up to 100 cycles, because the G/Si composites are uniformly dispersed and embedded in the CNF matrix. The effect of the G/Si composites on the electrochemical performance of the CCNFs with G/Si anode is investigated by microstructure analysis and electrochemical testing.

2. Experimental

2.1. Materials

PAN and *N,N*-dimethylformamide (DMF) were purchased from Aldrich Chemical Co. (USA) and were used as received without further purification. Si NPs (particle size 20–30 nm) were purchased from Nanostructured & Amorphous Materials, Inc. and graphite powder (crystalline, ~300 mesh, >99%, synthetic from desulfurized petroleum coke) was obtained from Alfa Aesar.

2.2. Preparation of G/Si composites

GO was synthesized from graphite according to the modified Hummers method [34,35]. Si NPs were prepared according to the classical Stöber method [36]. The Si NPs (0.5 g) were further dispersed into 60 mL toluene solution via sonication. After 30 min, 3 mL of 3-aminopropyl-trimethoxysilane (APS) was poured into the above solution and refluxed for 24 h under nitrogen atmosphere [37]. The products were washed with methanol/acetone and dried at 80 °C in a vacuum oven to obtain amine-functionalized Si NPs. G/Si were fabricated by the electrostatic interaction between negatively charged GO and positively charged amine-functionalized Si NPs in pH 2 aqueous solution. To 30 mL aqueous GO suspension was added 7 mg of amine-functionalized Si NPs under vigorous stirring at pH 2 solution for 1 h. After 1 h, 0.5 mL hydrazine (35 wt%) was added to this suspension to reduce GO to graphene. The obtained dark grayed dispersion was centrifuged and washed with deionized water to obtain G/Si composites.

2.3. Preparation of CCNFs with G/Si

Electrospinning solutions were prepared by dispersing an appropriate amount of G/Si composites (5, 10, and 20 wt% relative to PAN) into 10 wt% PAN solution in the DMF, and the solution was sonicated for 2 h in a bath-type sonicator to homogeneously disperse the G/Si composites. Electrospinning was conducted by applying a high positive voltage (20 kV) to the polymer solution via the tip of the syringe needle. The electrospun fibers were collected as a thin web on aluminum foil wrapped on a metal drum rotating at approximately 300 rpm. Oxidative stabilization was then performed using a conventional muffle furnace at 250 °C in air to induce thermal stability in the CCNFs. The CCNFs were then thermally treated at 800 °C, respectively, in an inert atmosphere. The CCNF with G/Si webs are designated as 5-GSP, 10-GSP, and 20-GSP, which indicates concentrations of 5, 10, and 20% G/Si composites relative to PAN, respectively. To compare the electrical properties, 20-SP (20 wt% Si NPs relative to PAN) and CNF (PAN-based CNFs) were prepared by the same electrospinning and heat treatment processes.

2.4. Characterization

The surface morphology of the nano-structured materials was examined by field emission scanning electron microscopy (FE-SEM, Hitachi, S-4700) equipped with energy dispersive X-ray spectroscopy (EDS). Transmission electron microscopy (TEM) images and selected area electron diffraction (SAED) micrographs were obtained with a Tecnai-F20 system operated at 200 kV at the Gwangju center of the Korea Basic Science Institute (KBSI), Korea. Samples for analysis were prepared on a carbon-coated Cu grid by dip-coating in dilute-appropriate solutions (~1.0 wt% solid content). X-ray diffraction (XRD) was obtained from ground-up samples of the fibers using a D-Max-2400 diffractometer and CuKα radiation ($\lambda = 0.15418$ nm). Backscattering Raman measurement was carried out with a Renishaw in Via-Reflex instrument at room temperature. A He–Ne laser was used to produce monochromatic red light of 633 nm wavelength at a power of approximately 15 mW on the sample surface.

2.5. Cell fabrication and measurement

The web-shaped CCNFs with G/Si were dried for 12 h at 120 °C in vacuum oven to completely remove the water. After drying, the CCNFs with G/Si were directly inserted into a 2032 coin cell (HohsenCorp.) to cut the webs into 15-mm-diameter circles. Polypropylene film (Celgard 2400) was used as a separator, and a mixed solution of 1 M $LiPF_6$ in ethylene carbonate (EC) and dimethylene carbonate (DMC) (1 M $LiPF_6$ + EC/DMC (1:1 vol%), Techno Semichem. Co.) was used as the liquid electrolyte. The coin cell was composed of CCNFs with G/Si as the working electrode and lithium foil as the counter electrode. The coin cell was assembled in an Ar-filled grove box. The galvanostatic discharge (lithium insertion)–charge (lithium extraction) properties of the samples were measured at a current density of 100 mA g^{-1} over a voltage range of 0.02–1.50 V. Our procedure did not require any polymer binder or conducting agent because these 1D porous CCNF webs with G/Si were directly used as anodes for LIBs due to the by adequate contact between the sample and the current collector.

3. Results and discussion

The G/Si composites were fabricated by wrapping Si NPs with GO, followed by GO reduction, as shown in Fig. S1. SEM analysis reveals that the fracture edges of the GO exhibit a layered structure

through the entire cross-section (Fig. S2a). TEM images of the GO reveal flexible, wrinkled, thin stacked sheets with a well-defined few layer structure in Fig. S2b [38,39]. XRD pattern and Raman spectroscopy of GO are presented in Fig. S3. For natural graphite, the characteristic peak of graphite at 26.48° corresponds to the (002) diffraction peak with an interlayer distance of 0.34 nm. For GO, the peak at 26.48° disappeared and an additional peak at 11.46° is observed, corresponding to the (001) diffraction peak and indicating a higher interlayer spacing of 0.77 nm, as evidenced from the XRD spectrum (Fig. S3a). The larger interlayer distance of GO is due to the formation of oxygen functional groups such as carboxyl and hydroxyl groups, which suggests that the original graphite powders had been almost completely oxidized [40–42]. The Raman spectrum of GO exhibits two large peaks in Fig. S3b: one near 1350 cm^{-1}, which is a D peak from the amorphous structures of carbon, and the other near 1590 cm^{-1}, which is a G peak from the graphitic structures of carbon [14,15].

The surface of GO was negatively charged due to the oxygen functional group such as carboxylic acid and hydroxyl groups at the surface and edge of the graphene sheets, while the amine-functionalized Si NPs were positively charged in pH 2 aqueous solution [37]. Therefore, the G/Si composites were fabricated by self-assembly between positively charged, amine-functionalized Si NPs and negatively charged GO, which is driven by the electrostatic interactions. The GO with the oxygen functional groups is capable of anchoring Si NPs without aggregation effects of Si NPs. Moreover the electrostatic repulsion among the positively charged, amine-functionalized Si NPs suppresses the growth and amalgamation of the Si NPs [43–45]. The amine-functionalized Si NPs keeps the surface morphology with spherical nanostructured in Fig. 1a. The SEM image, low- and high-magnification TEM images (Fig. 1b–d) of the G/Si composites show that the composites are composed of Si NPs and graphene sheets. In the SEM and TEM images, the neighboring Si NPs are firmly bounded and linked to the graphene sheets with numerous folds at the edges, indicating that the Si NPs are covered and wrapped with the sheet-like graphene that could adhere on the Si NPs, rather than wrapping each sphere. In addition, some corrugation of graphene sheet is detected, suggesting flexible and ultrathin structure of the graphene shells. Therefore, the graphene sheets wrapping the Si NPs help prevent agglomeration and ensure a good dispersion of these Si NPs over the graphene support [44–46].

Fig. 2 shows typical SEM images of 5-GPS, 10-GSP, and 20-GSP. All samples exhibit long and continuous cylindrical morphologies with homogeneously distributed diameters ranging from 200 to 250 nm. While the morphology of the 5-GSP, as shown in Fig. 2a, shows a relatively smooth surface, 10-GSP and 20-GSP in Fig. 2b and c shows rough surfaces with a large number of nodes or joints due to Si NP agglomeration as the G/Si content increases. In the case of the 20-SP (Fig. 2d), agglomerated Si clusters in the shape of bunches of grapes are exposed on the fiber surface. In comparison, Si agglomerations of 20-GSP are not observed along the exterior surface of the fiber and are embedded in the fiber, as shown in the inset of Fig. 2c and d, although they form some Si NP clusters at high G/Si concentrations. In the corresponding EDX spectrum, the individual fibers consist of C, O and Si and the atomic percent-ages of C, N, and Si in 10-GSP are estimated to be 78.83, 6.18, and 14.96%, respectively.

The TEM images were inspected to gain deeper insight of the distribution of Si NPs within the nanofibers in Fig. 3. The TEM images of 10-GSP (Fig. 3a) and 20-GSP (Fig. 3b) show that Si NPs are relatively embedded in the CCNFs although they are agglomerated to form some clusters, while significant aggregation is observed both inside and on the fiber surface for 20-SP (Fig. 3c). These SEM and TEM results indicate that the graphene of the G/Si composites helps disperse the non-agglomerated Si NPs inside the CNF matrix

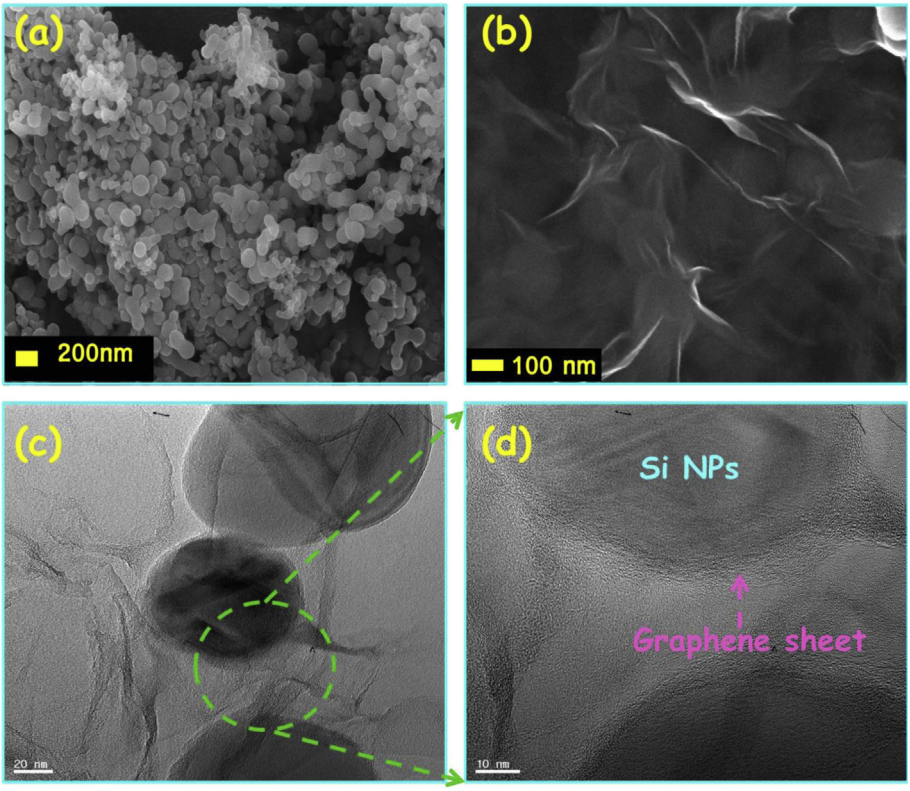

Fig. 1. SEM images of (a) amine-functionalized Si NPs and (b) G/Si composites, TEM images of G/Si composites of (c) low and (d) high magnifications.

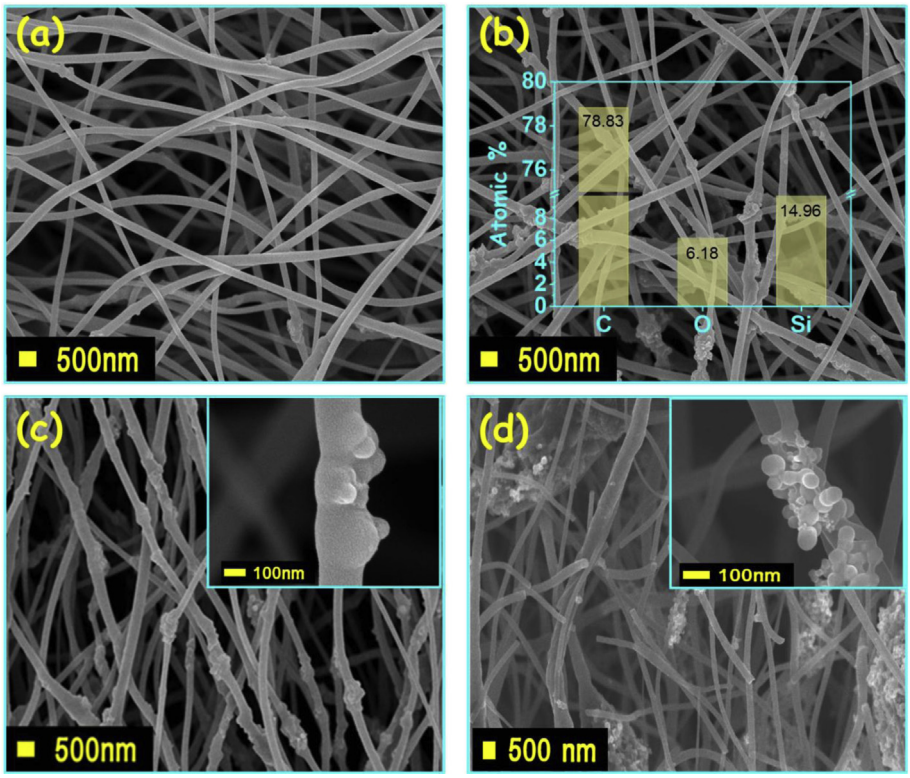

Fig. 2. FE-SEM images of (a) 5-GSP, (b) 10-GSP, (c) 20-GSP, (d) 20-SP.

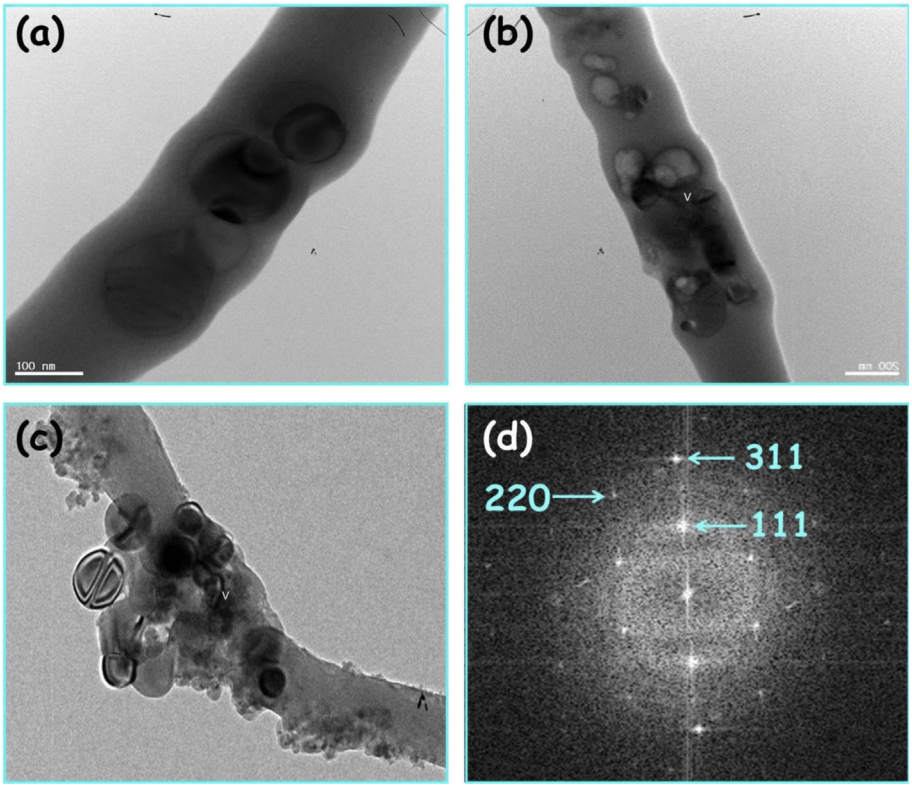

Fig. 3. TEM images showing (a) 10-GSP, (b) 20-GSP, and (c) 20-SP, and (d) SAED of 10-GSP.

from preventing inter-particle aggregation of Si NPs [44–46]. The corresponding selected area electron diffraction (SAED) pattern for 10-GSP in Fig. 3d can be indexed to the [111], [220] and [311] diffraction rings and is in good agreement with the face-centered cubic structure [47,48].

XRD measurements were conducted to evaluate the structure of various CCNFs with G/Si (GSP) and the G/Si composite, and the results are shown in Fig. 4. For the G/Si composite, the peak of GO at about 11.46° (Fig. S2a) has disappeared and a new peak has appeared between 20° and 30° and is assigned to the d_{002} layers, which indicates that GO has been reduced to graphene [20]. The XRD patterns (Fig. 4a) clearly show that the peaks at 28.4°, 48.1°, and 57.3° correspond to the (111), (220), and (311) diffraction of silicon (JCPDS 772107) for all the samples, respectively; this pattern implies the presence of polycrystalline Si in the amorphous carbon matrix [46]. In addition to the diffraction of Si, there are also broad diffraction peaks near 24.8° for various GSP, which was attributed to the disordered carbon that is attributed to CNFs [49]. In the Raman spectra (Fig. 4b), two main peaks are observed at approximately 1360 and 1580 cm^{-1}, which are designated as the D and G bands, respectively. The G band is associated with crystalline graphite, while the D band is attributed to amorphous graphitic materials [32]. The Raman spectra of all the samples exhibit strong and sharp peaks at around 498 and 300 cm^{-1}, corresponding to the characteristic peaks of microcrystalline Si [50].

The electrochemical performance of the various GSP anodes was evaluated and compared by carrying out Galvanostatic charge–discharge experiments at a current density of 100 mA g^{-1} between 0.02 and 1.50 V. Fig. 5 shows the 1st and 2nd charge–discharge behaviors of CNF, 5-GSP, 10-GSP, 20-GSP, and 20-SP electrodes using a cell assembled with Li. During the first discharge process, a potential plateau at around 0.6 V and a sloping voltage range (0.6–0.01 V) are observed for various anodes. The first plateau is related to the decomposition of the electrolyte and the formation of the solid electrolyte interphase (SEI) [22,51,52] and the peak below 0.6 V corresponds to the insertion of lithium in the various anodes [32,53]. The anodes made from CNFs show a much higher specific discharge capacity of ca. 767 mAh g^{-1} at the first cycle compared with the 372 mAh g^{-1} theoretical value of graphite (Fig. 5a). The first discharge and charge capacities are 626 and 298 mAh g^{-1} for 5-GSP (Fig. 5a), 778 and 440 mAh g^{-1} for 10-GSP (Fig. 5b), and 923 and 602 mAh g^{-1} for 20-GSP (Fig. 5c) electrodes, respectively. Moreover, 20-SP with none wrapped silicon possesses an initial reversible capacity of over 1310 mAh g^{-1} and a coulomb efficiency of 82%. These results indicate that the 20-GSP and 20-SP anode with higher capacity Si NPs showed the highest capacity and largest coulombic efficiency. Moreover, in the 1st cycle, the irreversible capacity loss can be attributed to the formation of an SEI passivation layer on the surface of electrode [32,46]. However, a high coulombic efficiency of more than 90% was obtained for all electrodes in the second cycle because the microstructure of the GSP was stabilized, leading to the reversible lithiation and delithiation reactions that occur upon the discharge and charge processes in the subsequent cycles.

Fig. 6 shows the differential capacity curves of the 20-GSP anode after the 1st, 2nd, 10th, 20th, and 50th cycles between 0.02 and 1.4 V at a current of 100 mA g^{-1}. In the first charging, the irreversible cathodic peak developed at around 0.64 V was attributed to electrolyte decomposition and the formation of SEI layers [28]. The strong peak below 0.1 V indicates that the crystalline Si transforms to amorphous Si by the lithiation after the first cycle and the Li ions are intercalated/de-intercalated into the disordered CNF matrix [54]. In the subsequent cycles, several peaks originate from the phase transitions of Li_xSi and Si are developed [52]. The peaks located at 0.3, 0.24 and 0.08 V in the cathodic branches correspond to the reaction of Li ion with amorphous Si during discharging. Furthermore, the two anodic peaks located at 0.29 and 0.45 V are attributed to the de-alloying process of Li_xSi alloys with different compositions during charging [55]. Therefore, the differential capacity curves demonstrate the excellent capacity retention of the composite with cycling, indicative of good anode stability [56].

The reversible capacities as a function of cycle number for various GSPs, 20-SP, and CNFs are compared at a constant current of 100 mA g^{-1} in Fig. 7. Fig. 7 shows that the cycle life decreases in the following order: 20-GSP > 10-GSP > 5-GSP > CNF > 20-SP. In all 50 cycles, the anodes made from 20-GSP show the largest capacities and the best cycling stability. Although the discharge capacity of 20-GSP is just 66.3% of the initial value at the 50th cycle, it is still much larger than the 372 mA g^{-1} theoretical value of graphite. In addition, the specific discharge capacity of 20-SP is drastically decreased from 1583 to 146 mA g^{-1} to the 50th cycle, corresponding to a 9.2% capacity retention, due to the volume expansion by Li_xSi formation during the continuous charge–discharge process. The high cycling performance and superior reversible capacity of the 20-GSP anode can be attributed to the one-dimensional nanofibrous structure with non-agglomerated Si NPs in the CNF matrix. For 20-GSP, the Si NPs wrapped by graphene are dispersed within the CNFs, which prevents the aggregation and mechanical stress of Si NPs during lithiation and delithiation. In addition, graphene and CNF can supply excellent conductivity to promote charge transfer and maintain a stable electrical contact, which preserves the integrity of the electrode during cycling [32,57–60].

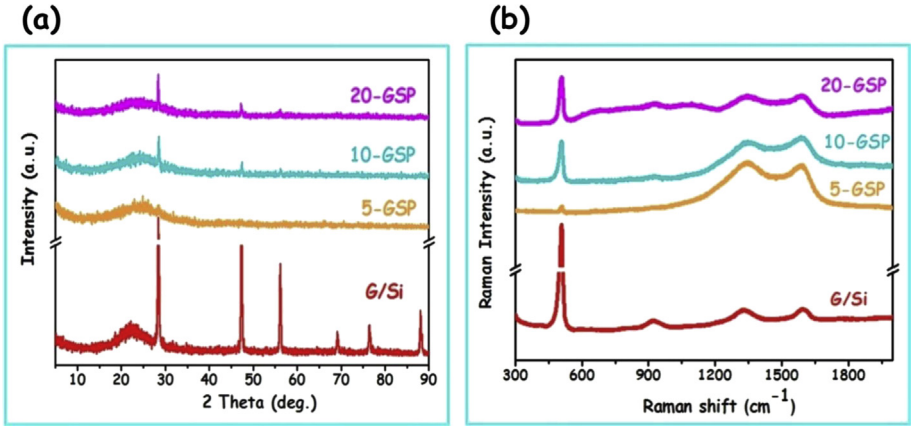

Fig. 4. (a) XRD patterns and (b) Raman spectra of G/Si, 5-GSP, 10-GPS, and 20-GSP.

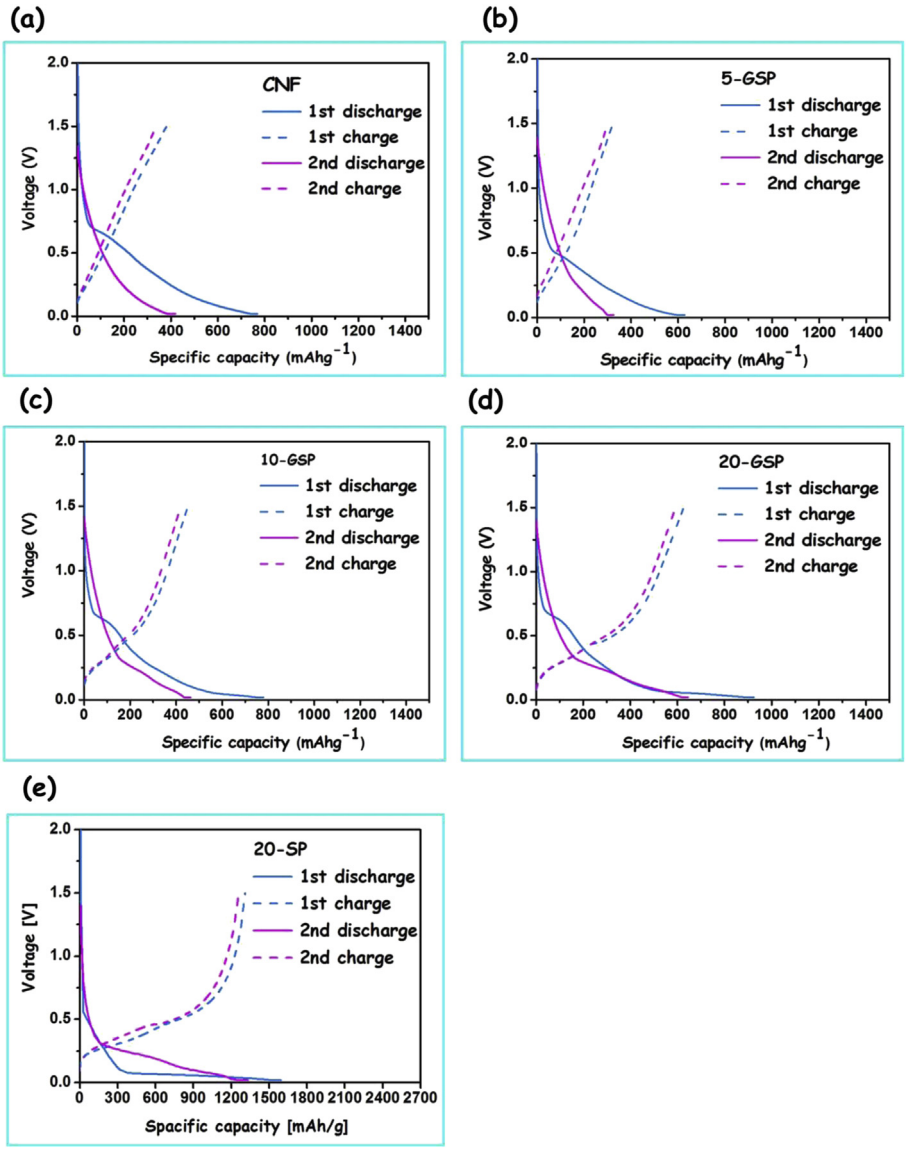

Fig. 5. Voltage profiles of CCNFs with G/Si in 1 M $LiPF_6$/EC/DMC at 100 mA g^{-1} current density: (a) CNF, (b) 5-GSP, (c) 10-GSP, (d) 20-GSP, and (e) 20-SP.

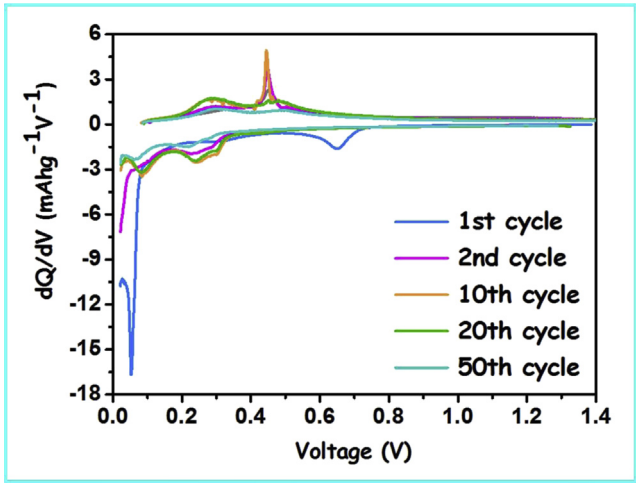

Fig. 6. Differential capacity vs. cell potential curves of the 20-GSP electrode after 1st, 2nd, 10th, 20th, and 50th cycles.

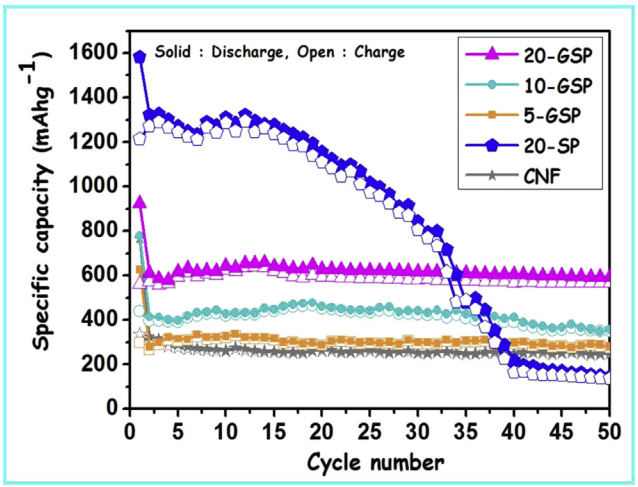

Fig. 7. Cycling performance of various CCNFs with G/Si, 20-SP, and CNF.

As a result, the volume expansion and shrinkage of Si NPs are somewhat overcome for 20-GSP, despite the high Si NP contents because of the good dispersion of Si NPs and the buffer effects of the carbon matrix, which leads to a high specific discharge capacity and good capacity retention. However, in the case of the 20-SP electrode, the exposed agglomerated Si clusters on the fiber surface contact the electrolyte directly, which prevents the formation of an SEI passivation layer on the silicon surface, and induces the volume expansion of the Si NPs, giving rapid capacity fading [57,60].

The Nyquist plots in Fig. S4 show that the electrochemical impedance behaviors for CNF, 5-GSP, 10-GSP, and 20-GSP with amplitude of 10 mV over the frequency range 100 kHz–10 mHz to elucidate their interfacial properties. In the high frequency range, the semicircle indicates charge transfer resistance, i.e., the migration rate of ions at the interface between the solution and the electrode surface. A single semicircle that intercepts the Re(Z) axis at R_s (electrolyte resistance) and $R_s + R_{ct}$ (charge-transfer resistance) is observed in the high-frequency region. The R_{ct} of the CNF, 5-GSP, 10-GSP, and 20-GSP electrodes was calculated as 53.85, 39.69, 31.72, and 29.09 Ω, respectively. The low value, R_{ct}, of the 20-GSP electrode can be explained by the more numerous electrochemical active sites and the large contact area with the electrolyte for charge transfer reactions, which ensures good electronic contact between the Si NPs and the CNF matrix, due to the high contents of G/Si composites embedded within the CNF matrix [20,61,62]. Therefore, 20-GSP with low charge transfer resistance at the interface of the electrolyte and active material contributes to the high electrochemical performance with highly reversible capacity and excellent cyclability.

Fig. 8 shows the SEM images of the surface of the 5-GSP, 10-GSP, and 20-GSP electrodes after 50 cycles of charging/discharging. Compared with the SEM images of CCNFs with G/Si before cycling (inset figs), some nodes or joints with mushroom-shaped structures have appeared in the cycled nanofibers, due to the volume expansion and shrinkage upon repeated lithium insertion/extraction. However, the long and continuous structure of CNF remains in the cycled nanofibers, without disruption in the fibers, indicating that the integrity of the CNFs is preserved during the charge/discharge cycles. These results reveal that the CNFs in GSP can help to maintain good contact with both the active materials and the electrolyte after lithium insertion and extraction cycles and buffer the Si volume expansion during the lithium insertion and extraction processes [23,30,31].

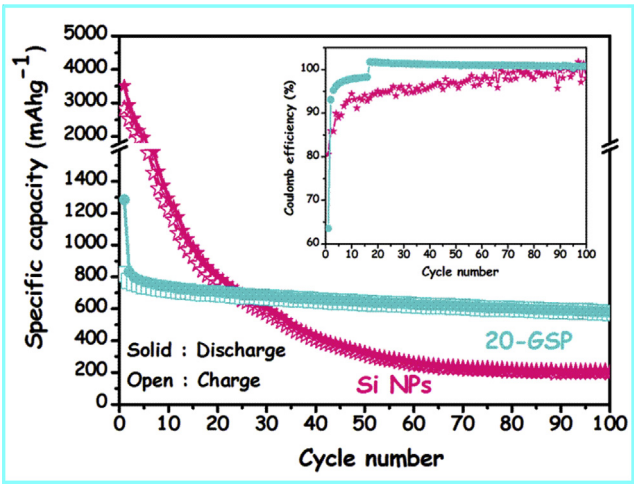

Fig. 9. Discharge capacity and coulombic efficiency vs. cycle number of the Si NPs and ground 20-GSP electrodes at 100 mA g^{-1} current density in 1 M $LiPF_6$/EC/DMC.

Since Si NPs are an attractive candidate as an anode material due to high theoretical lithium capacity, the Si/C composites were examined as an anode. In particular, the Si/C composites were prepared to match the weight ratio of silicon and carbon in 20-GSP as follows: The silicon material (20 wt%) is mixed with 80 wt% of a

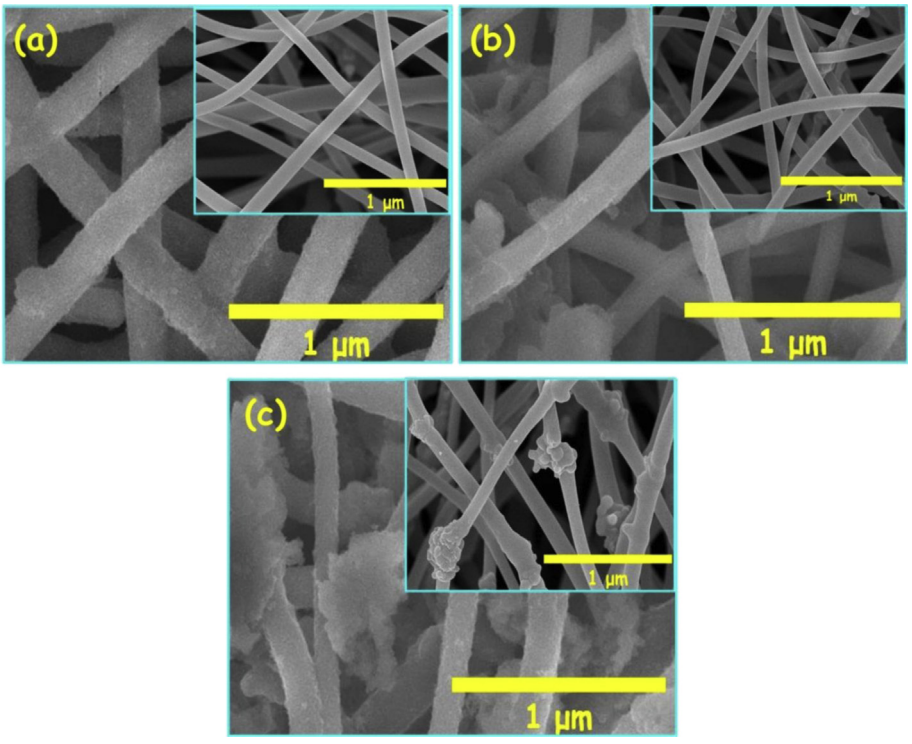

Fig. 8. SEM images of (a) 5-GSP, (b) 10-GSP, and (c) 20-GSP PVSi-20 electrodes after 50 cycles. The insets show the SEM images of CCNFs with G/Si before cycling.

natural graphite with a size of about 15–17 μm (provided by Poscochemtech, Korea). The web-structured 20-GSP was ground in order to understand the electrochemical performance of Si/C composites. The Si/C composites and ground 20-GSP electrodes were prepared using the traditional method, i.e., the mixing anode active material (80 wt%) with polyacrylic acid binder (10 wt%) and Super-P conductor (10 wt%), mixed thoroughly and coated onto a copper foil which serves as current collector. The area loading is 1.5 mg cm^{-2}. Fig. 9 shows the cycling performance and coulombic efficiency for the Si/C composites and the ground 20-GSP electrodes at the current density of 100 mA g^{-1} at the voltage ranging from 0.02 to 1.50 V. The capacities of the Si/C composites and ground 20-GSP decrease from 3059 and 1240 mAh g^{-1} to 203 and 612 mAh g^{-1}, which correspond to capacity retentions of 6.6 and 50.0% after the 100th cycle, respectively. For the ground 20-GSP electrode, the coulombic efficiency reaches 96.1% at the 2nd cycle and remains close to 100% after the 100th cycle, exhibiting excellent cyclic performance. The initial specific capacity of the Si/C composites is higher than that of the ground 20-GSP electrode, but the specific discharge capacity of the Si/C composites drops dramatically to 203 mAh g^{-1} at the 100th cycle.

The SEM images of ground 20-GSP and the Si/C composites before and after 100 cycles are shown in Fig. 10, to elucidate the microstructural change and the mechanical stability. The ground 20-GSP anode keeps the homogeneous surface morphology with no apparent cracks after 100 cycles in Fig. 10a and b. The ground 20-GSP electrodes were not collapsed or severely pulverized, and the electrode volume was even expanded from 11.5 to 21.0 μm after 100 cycles in the inset figs of Fig. 10a and b. However, the Si/C composites exhibited structural failure with many cracks and particles on the cycled electrode surface, compared to the uncycled electrode in Fig. 9c and d. In addition, we could not identify the cross-sectional SEM image of the cycled the Si/C composite electrode, due to the detachment of the electrode from the substrate. This phenomenon was caused by the large volume change and high mechanical stress in the alloying/de-alloying process, leading to its pulverization and loss of electrical contact between the active particles, and hence to rapid capacity fading.

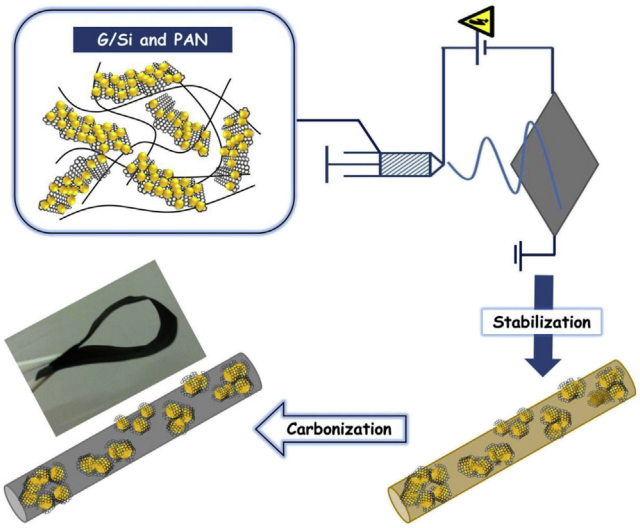

Fig. 11. Illustration of the preparation of G/Si-embedded carbon composite nanofibers (CCNFs with G/Si).

Fig. 11 represents the preparation method of the CCNFs with G/Si. The flexible nanofiber webs with well-dispersed G/Si was prepared using electrospinning followed by thermal treatment. The graphene of the G/Si composites helps the dispersion of the non-agglomerated Si NPs inside the CNF matrix by preventing inter-particle aggregation of the Si NPs. Fig. S5 shows the nitrogen adsorption–desorption isotherms of 20-GSP and CNF. The adsorption isotherms of 20-GSP and CNF showed typical type I behavior, indicating high microporosity, and the adsorption of

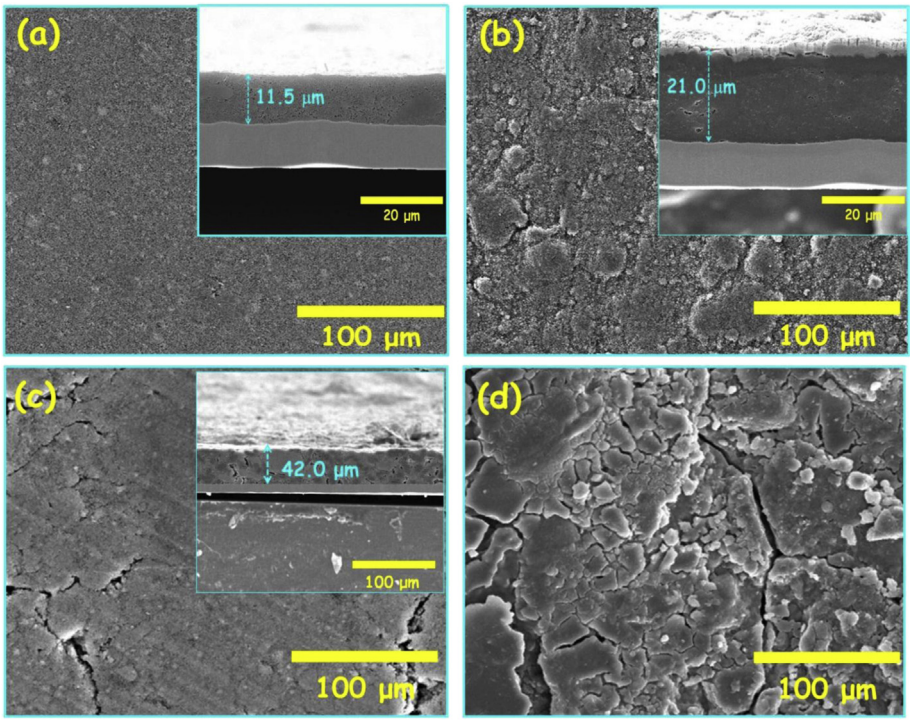

Fig. 10. Top view SEM images of (a) 20-GSP, and (b) Si NPs before cycling; and of (c) 20-GSP, and (d) Si NPs after the 100th cycle. The insets show the cross-sectional SEM images.

nitrogen was almost complete at a low relative pressure, $P/P0 < 0.1$. The specific surface area increased from 180 $m^2\ g^{-1}$ for CNF to 230 $m^2\ g^{-1}$ for 20-GSP. Therefore, high specific area of 20-GSP increases the contact area of electrode and electrolyte and supply extra sites to storage lithium, leading to higher charge/discharge rates and electrochemical performance. In addition, the CNF and graphene plays a very important role as buffering agent to prevent Si NPs from agglomerating and an electrical conductor to promote charge transfer in improving the electrochemical performance. Therefore, it can be concluded that the introduction of graphene and CNF in ground 20-GSP helps to ensure stable cycle performance while maintaining the electrode morphology by integral and continuous electric contact networks around the Si particles, even when they are slightly expanded during lithiation and delithiation [63]. Further studies are required to provide more dispersal of the Si NPs in the carbon matrix using the protective polymer or amorphous SiO_x as alternative anode material with a high specific capacity, good reversibility, and excellent cycle retention.

4. Conclusions

Bendable CCNFs with G/Si were produced by incorporating G/Si composites into PAN through one-step electrospinning followed by thermal treatment, and their electrochemical properties as an LIB anode were investigated. The graphene of the G/Si composites helps the dispersion of the non-agglomerated Si NPs inside the CNF matrix by preventing inter-particle aggregation of the Si NPs. The 20-GSP electrode exhibited a reversible capacity of above 600 mAh g^{-1} up to 100 cycles and stable capacity retention, which was superior to those of 20-SP and Si NPs. In addition, 20-GSP maintained morphological stability and structural integrity after 100 electrochemical charge/discharge cycles. The high cycling performance and superior reversible capacity of the 20-GSP anode was attributed to the one-dimensional nanofibrous structure with non-agglomerated Si NPs in the CNF matrix. The Si NPs wrapped by graphene were dispersed within the CNFs, which prevented the aggregation and mechanical stress of Si NPs during lithiation and delithiation. In addition, the graphene and CNF matrix afforded excellent conductivity by promoting charge transfer, maintaining a stable electrical contact, and buffering the Si volume expansion, which preserved the integrity of the electrode during cycling. These study results supported the promising potential of the electrospun CCNFs with G/Si as an anode material for LIBs with high specific capacity, good reversibility, and excellent cycle performance.

Appendix A. Supplementary data

Supplementary data related to this article can be found at http://dx.doi.org/10.1016/j.jpowsour.2014.09.109.

References

[1] B. Gao, S. Sinha, L. Fleming, O. Zhou, Adv. Mater. 13 (2001) 816.
[2] C.K. Chan, H.L. Peng, G. Liu, K. McIlwrath, X.F. Zhang, R.A. Huggins, Y. Cui, Nat. Nanotechnol. 3 (2008) 31.
[3] T.H. Hwang, Y.M. Lee, B.-S. Kong, J.-S. Seo, J.W. Choi, Nano Lett. 12 (2012) 802.
[4] R. Lv, J. Yang, P. Gao, Y. Li, J. Wang, J. Alloys Compd. 490 (2010) 84.
[5] M. Egashira, H. Takatsuji, S. Okada, J.-I. Yamaki, J. Power Sources 107 (2002) 56.
[6] J.-T. Li, S.-R. Chen, X.-Y. Fan, L. Huang, S.-G. Sun, Langmuir 23 (2007) 13174.
[7] K.T. Lee, Y.S. Jung, S.M. Oh, J. Am. Chem. Soc. 125 (2003) 5652.
[8] G. Derrien, J. Hassoun, S. Panero, B. Scrosati, Adv. Mater. 19 (2007) 2336.
[9] K. Zhong, Z. Xia, B. Zhang, H. Li, Z. Wang, L. Chen, J. Power Sources 195 (2010) 3300.
[10] D. Deng, J.Y. Lee, Chem. Mater. 20 (2008) 1841.
[11] S.-M. Paek, E.J. Yoo, I. Honma, Nano Lett. 9 (2009) 72.
[12] P. Poizot, S. Laruelle, S. Grugeon, L. Dupont, J.M. Tarascon, Nature 407 (2000) 496.
[13] K.T. Nam, D.W. Kim, P.J. Yoo, C.Y. Chiang, N. Meethong, P.T. Hammond, Y.M. Chiang, A.M. Belcher, Science 312 (2006) 885.
[14] Y.G. Li, B. Tan, Y.Y. Wu, Nano Lett. 8 (2008) 265.
[15] M.V. Reddy, T. Yu, C.H. Sow, Z.X. Shen, C.T. Lim, G.V.S. Rao, B.V.R. Chowdari, Adv. Funct. Mater. 17 (2007) 2792.
[16] J. Chen, L.N. Xu, X.Y. Li, X.L. Gou, Adv. Mater. 17 (2005) 5826.
[17] Z.M. Cui, L.Y. Hang, W.G. Song, Y.G. Guo, Chem. Mater. 21 (2009) 1162.
[18] L.J. Zhi, Y.S. Hu, B.E. Hamaoui, X. Wang, I. Lieberwirth, U. Kolb, J. Maier, K. Mullen, Adv. Mater. 20 (2008) 1727.
[19] T. Tran, K. McCormac, J. Li, Z. Bi, J. Wu, Electrochim. Acta 117 (2014) 68.
[20] Y.-S. He, P. Gao, J. Chen, X. Yang, X.-Z. Liao, J. Yang, Z.-F. Ma, RSC Adv. 1 (2011) 958.
[21] L.-F. Cui, Y. Yang, C.-M. Hsu, Y. Cui, Nano Lett. 9 (2009) 3370.
[22] Y.S. Hu, R. Demir-Cakan, M.M. Titirici, J.O. Muller, R. Schogl, M. Antonietti, J. Maier, Angew. Chem. Int. Ed. 47 (2008) 1645.
[23] L. Ji, X. Zhang, Electrochem. Commun. 11 (2009) 1146.
[24] R.D. Cakan, M.M. Titirici, M. Antonietti, G.L. Cui, J. Maier, Y.S. Hu, Chem. Commun. (2008) 3759.
[25] S.H. Ng, J. Wang, D. Wexler, K. Konstantinov, Z.P. Guo, H.K. Liu, Angew. Chem. Int. Ed. 45 (2006) 6896.
[26] M. Holzapfel, H. Buqa, W. Scheifele, P. Novák, F.M. Petrat, Chem. Commun. (2005) 1566.
[27] Z.P. Guo, D.Z. Jia, L. Yuana, H.K. Liu, J. Power Sources 159 (2006) 332.
[28] L. Wang, C.X. Ding, L.C. Zhang, H.W. Xu, D.W. Zhang, T. Cheng, C.H. Chen, J. Power Sources 195 (2010) 5052.
[29] P.J. Zuo, G.P. Yin, Z.L. Yang, Z.B. Wang, X.Q. Cheng, D.C. Jia, C.Y. Du, Mater. Chem. Phys. 115 (2009) 7570.
[30] Q. Si, K. Hanai, T. Ichikawa, A. Hirano, N. Imanishi, Y. Takeda, O. Yamamoto, J. Power Sources 195 (2010) 1720.
[31] L. Ji, X. Zhang, Carbon 47 (2009) 3219.
[32] L. Ji, K.-H. Jung, A.J. Medford, X. Zhang, J. Mater. Chem. 19 (2009) 4992.
[33] Y.H. Jane, J.B. David, Q. Yue, M.M. Harry, N.G. Maryam, A.C.P. Nazri Andrew, D.L. Patrick, J. Power Sources 221 (2013) 455.
[34] W.S. Hummers, R.E. Offeman, J. Am. Chem. Soc. 80 (1958) 1339.
[35] Y.Y. Liang, J. Frisch, L.J. Zhi, H.X. Norouzi-Arasi, L. Feng, J.P. Rabe, N. Koch, K. Müllen, Nanotechnology 20 (2009) 434007.
[36] W. Stober, A. Fink, E. Bohn, J. Colloid Interface Sci. 26 (1968) 62.
[37] S. Yang, X. Feng, X. Ivanovici, K. Mllen, Angew. Chem. Int. Ed. 49 (2010) 8408.
[38] H. Chen, M.B. Muller, K.J. Gilmore, G.G. Wallace, D. Li, Adv. Mater. 20 (2008) 3557.
[39] N.I. Kovtyukhova, P.J. Ollivier, B.R. Martin, T.E. Mallouk, S.A. Chizhik, E.V. Buzaneva, A.D. Gorchinskiy, Chem. Mater. 11 (1999) 771.
[40] X. Tong, H. Wang, G. Wang, L. Wan, Z. Ren, J. Bai, J. Solid State Chem. 184 (2011) 982.
[41] W. Chen, L. Yan, Nanoscale 2 (2010) 559.
[42] C. Fu, G. Zhao, H. Zhang, S. Li, Int. J. Electrochem. Sci. 8 (2013) 6269.
[43] S.A. Ju, K. Kim, J.-H. Jun, S.-S. Lee, ACS Appl. Mater. Interfaces 3 (2011) 2904.
[44] J.S. Lee, K.H. You, C.B. Park, Adv. Mater. 24 (2012) 1084.
[45] S.Y. Kim, B.-H. Kim, K.S. Yang, K.-Y. Kim, Mater. Lett. 71 (2012) 74.
[46] G. Zhou, D.-W. Wang, F. Li, L. Zhang, N. Li, Z.-S. Wu, L. Wen, G.Q. Lu, H.-M. Cheng, Chem. Mater. 22 (2010) 5306.
[47] J. Zou, P. Sanelle, K.A. Pettigrew, S.M. Kauzlarich, J. Cluster Sci. 17 (2006) 565.
[48] Y. Li, B. Guo, L. Ji, Z. Lin, G. Xu, Y. Liang, S. Zhang, O. Toprakci, Y. Hu, M. Alcoutlabi, X. Zhang, Carbon 51 (2013) 185.
[49] Z.P. Guo, E. Milin, J.Z. Wang, J. Chen, H.K. Liu, J. Electrochem. Soc. 152 (2005) A22116.
[50] W. Zhang, S. Znang, Y. Liu, T. Chen, J. Cryst. Growth 311 (2009) 1296.
[51] Q. Wang, L. Liu, L. Chen, X. Huang, J. Electrochem. Soc. 151 (2004) A1333.
[52] G. Maurin, C. Bousquet, F. Henn, P. Bernier, R. Almairac, B. Simon, Chem. Phys. Lett. 312 (1999) 14.
[53] G. Zou, D. Zhang, C. Dong, H. Li, K. Xiong, L. Fei, Y. Qian, Carbon 44 (2006) 828.
[54] B.-S. Lee, S.-B. Son, K.-M. Park, J.-H. Seo, S.-H. Lee, I.-S. Choi, K.-H. Oh, W.-R. Yu, J. Power Sources 206 (2012) 267.
[55] Z. Lu, L. Zhang, X. Liu, J. Power Sources 195 (2010) 4304.
[56] M.K. Datta, P.N. Kumta, J. Power Sources 158 (2006) 557.
[57] L. Chen, X. Xie, B. Wang, K. Wang, J. Xie, Mater. Sci. Eng. B 131 (2006) 186.
[58] H.-R. Jung, W.-J. Lee, J. Electrochem. Soc. 158 (2011) A644.
[59] T. Zhang, J. Gao, L.J. Fu, L.C. Yang, Y.P. Wu, H.Q. Wu, J. Mater. Chem. 17 (2007) 1321.
[60] S.Y. Kim, B.-H. Kim, K.S. Yang, J. Electroanal. Chem. 705 (2013) 52.
[61] H.-R. Jung, W.-J. Lee, Solid State Ionics 187 (2011) 50.
[62] Y. Zhang, X.G. Zhang, H.L. Zhang, Z.G. Zhao, F. Li, C. Liu, H.M. Cheng, Electrochim. Acta 51 (2006) 4994.
[63] H.-R. Jung, W.-J. Lee, J. Electroanal. Chem. 662 (2011) 334.